Phase behavior and characterization of heptamethyltrisiloxane-based de Vries smectic liquid crystal by electro-optics, x rays, and dielectric spectroscopy

S. P. Sreenilayam, D. M. Agra-Kooijman, V. P. Panov, V. Swaminathan, J. K. Vij, Yu. P. Panarin, A. Kocot, A. Panov, D. Rodriguez-Lojo, P. J. Stevenson, Michael R. Fisch, and Satyendra Kumar

Phys. Rev. E **95**, 032701 — Published 10 March 2017

DOI: 10.1103/PhysRevE.95.032701

The Phase behaviour and the characterization of heptamethyltrisiloxane based de-Vries SmA* liquid crystal by electro-optics, x-rays and dielectric spectroscopy

S. P. Sreenilayam[a], D. M. Agra-Kooijman[b†], V. P. Panov[a], V. Swaminathan[a], J. K. Vij[a*], Yu. P. Panarin[a, c], , A. Kocot[d], A. Panov[e], D. Rodriguez-Lojo[e], P. J. Stevenson[e], M. Fisch[b§] and Satyendra Kumar[b,f]

[a]Department of Electronic and Electrical Engineering, Trinity College,-The University of Dublin, Dublin 2, Ireland

[b†]Department of Physics and [§]College of Applied Engineering Sustainability and Technology Kent State University, Kent, OH 44242

[c]School of Electrical and Electronic Engineering, Dublin Institute of Technology, Dublin 8, Ireland

[d]Institute of Physics, Silesian University, Katowice, Poland

[e]School of Chemistry and Chemical Engineering, Queens University, Belfast, BT7 1NN, U. K.

[f]Division of Research and Department of Physics, University at Albany, Albany, NY 12222

A heptamethyltrisiloxane liquid crystal (LC) exhibiting Iso-SmA*- SmC* phases has been characterized by calorimetry, polarizing microscopy, x-ray diffraction, electro-optics and dielectric spectroscopy. Observations of a large electro-clinic effect, a large increase in the birefringence (Δn) with electric field, a low shrinkage in the layer thickness(~1.75%) at 20 ^{0}C below the SmA* to SmC* transition, and low values of the reduction factor (~0.40) suggest that SmA* phase in this material is of the de-Vries type. The reduction factor is a measure of the layer shrinkage in SmC* phase and it should be zero for an ideal de-Vries. Moreover, a decrease in the magnitude of Δn with decreasing temperature indicates the presence of the temperature-dependent tilt angle in the SmA* phase. The electro-optic behavior is explained by the generalized Langevin-Debye model as given by Shen et al. [Phys. Rev. E **88**, 062504 (2013)]. The soft mode dielectric relaxation strength shows a critical behavior when the system goes from SmA* to SmC* phase.

*Corresponding Author: jvij@.tcd.ie

1. INTRODUCTION

In liquid crystalline (LC) compounds, the phase transition from the orthogonal (SmA) to tilted (SmC) smectic phases is associated with an appearance of tilt (θ) between the molecular long axis $\boldsymbol{n}$ and layer normal $\boldsymbol{z}$ (Fig. 1a) Due to this tilt, the layer spacing in the SmC phase (d_C) is smaller than in SmA (d_A). In the realm of the rigid-rod molecular model being valid (Fig. 1a), the smectic layer thickness d_C is reduced from d_A by $\cos\theta$ [1-3]. In conventional SmC LCs, θ varies from zero to ~30º depending on temperature. The large layer contraction in ferroelectric SmC* induces chevron structures which in turn results into zigzag defects [4]. These defects present a roadblock to a successful commercialization of the ferroelectric LC (FLC) devices. The FLC devices intrinsically have faster switching modes [5] than their nematic counterparts that are currently predominantly used in the industry. The objective is therefore to eliminate these zigzag defects by making the smectic layer thickness almost independent of temperature so as to have the most desirable features of FLCs in the next generation of displays.

In 1972, Diele et al. reported a non-chiral LC with the same layer spacing in the SmC and SmA [6]. To explain it, de-Vries proposed a new type of SmA phase where the molecules are tilted as in SmC with two possible structures. In one case [7,8], SmC-like layers are stacked in a random fashion. In other words tilt directions with the same tilt angle in different layers are randomly oriented. This implies that the azimuthal angle (φ) varies randomly from on layer to next: no long range correlations in the azimuthal angle of the smectic layers was proposed to exist in this case. In the second model of de-Vries [9], the molecules are tilted and the correlation in the tilt direction exists within a single layer too, i.e. φ has a finite-correlation length. If the correlation length is much smaller than wavelength of the visible light, then the phase in optical experiments should behave as 'a uniaxial SmA'. The results of both de-Vries models should be that the directors in SmA phase would be distributed on to a cone as shown in Fig. 1b.

The chiral de-Vries materials show electro-optic behavior due to the field-induced azimuthal reorientation of the molecules on the cone and the apparent tilt angle measured by an optical experiment in SmA thus increases with the field. They exhibit a significantly large electroclinic effect due to the azimuthal reorientation and the induced tilt becomes saturated at "high" electric fields once the degeneracy in the azimuthal angle is lost (the azimuthal angle is condensed to values within narrow limits). For the zero external field, the maximum of the molecular orientational distribution function is at the cone angle (volcano distribution) rather than at the layer normal. The de-Vries behavior can be described by the reduction factor defined

as, $R = \frac{\delta(T)}{\theta_{opt(T)}} = \cos^{-1}[d_C(T)/d_{AC}]/\theta_{opt}(T)$; where $\delta(T)$ is the tilt angle for the layer shrinkage relative to layer thickness d_{AC} at the smectic A-C transition and θ_{opt} is the optical tilt angle determined by the polarizing optical microscopy [10, 11]. An ideal de-Vries material producing defect-free bookshelf geometry in SmC* phase will have the reduction factor R=0.

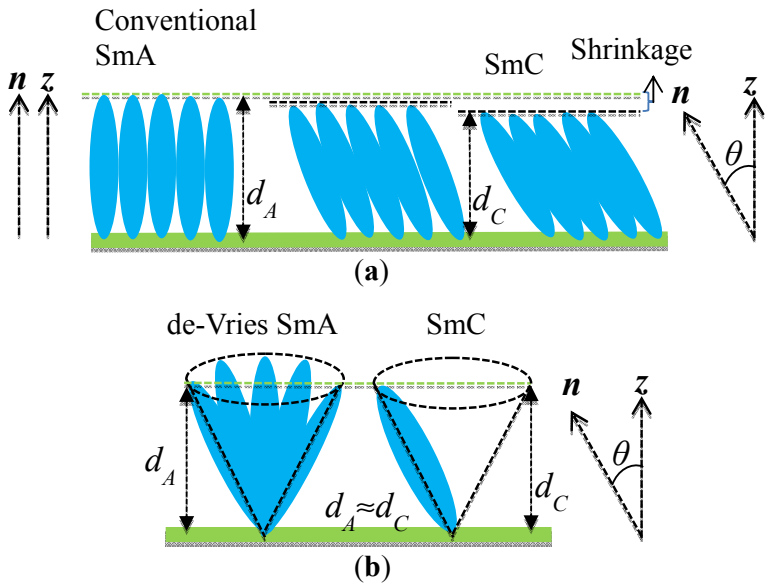

FIG. 1: Schematic representation of (**a**) conventional SmA-SmC (rigid rod model) and (**b**) de-Vries SmA-SmC (diffuse cone model) phase transition. Here, $\boldsymbol{z}$ is the layer normal, $\boldsymbol{n}$ is the molecular long axis orientation, θ is the angle between $\boldsymbol{n}$ and $\boldsymbol{z}$, d_C and d_A are the layer spacings in SmC and SmA phases, respectively.

Several research groups reported de-Vries type behavior in smectic LCs composed of non-chiral [12-14] and chiral [15-19] molecules. LC materials that behave as 'good de-Vries like' so far are siloxane-terminated TSiKN65 compound [20], its carbosilane-terminated analogue W599 [21] and the 2-phenylpyrimidine derivative 8422[2F3] [22]. For these materials, the layer contraction at the smectic A*–C* transition lies in the range of 0.65 to 1%. In this paper, we present experimental results on the calorimetric, optical, polarization measurements, dielectric spectroscopy and x-ray diffraction on heptamethyl- trisiloxane derivative MSi_3MR11, which exhibits a strong electroclinic effect with birefringence strongly increasing at SmA* - SmC* phase transition. Experimental results suggest that the SmA* phase in this material is of de-Vries type. The reduction factor for this material is found to be ~0.40. The electro-optic response and the induced polarization are found to be in agreement with the generalized Langevin-Debye model. The soft mode relaxation strength of de-Vries type SmA* phase as a function of temperature exhibits critical nature when the system undergoes a transition to SmC* phase.

2. EXPERIMENTAL

The molecular structure and the transition temperatures of the MSi_3MR11 are shown in Fig. 2a. This compound was resynthesized and it has two chiral centres. The synthetic procedure is given in the appendix A. One of the objectives here is to see whether two chiral centres give rise to a similar phenomenon as compounds with one chiral centre. The mesogenic core of MR11 consists of a biphenyl 2-chloro-3-methylpentanoate unit. Here 'M (mono-substituted)'stands for the number of siloxane end groups attached to the mesogen MR11. The mesogen MR11 [23] with 11 methylene units is attached to a trisiloxane backbone. The purity of the sample was found to much higher through its analysis by NMR than for the previously synthesized sample [23]. An analysis for the purity of the sample is given in the appendix A. The transition temperatures (Fig. 2a) are obtained on cooling under quasi-equilibrium condition with a cooling rate of ~1°C min^{-1} using polarizing microscopy.

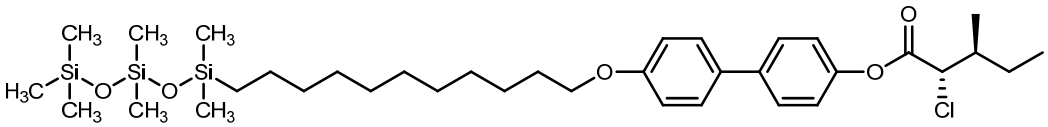

(**a**)

Cr **16ºC** [-5.12 J/g] SmC* **47ºC** [-1.06 J/g] SmA* **59ºC** [-5.56 J/g] Iso

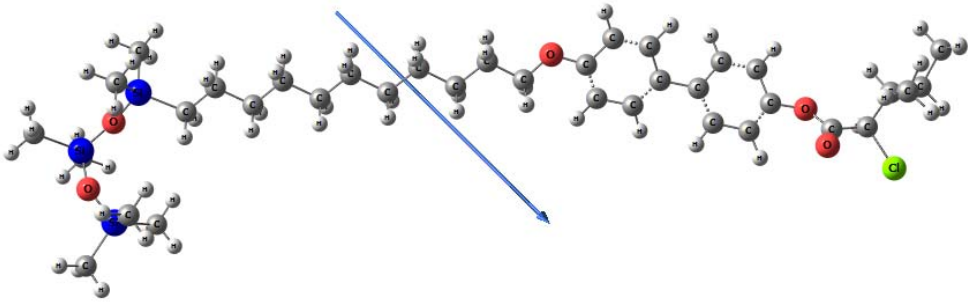

(**b**)

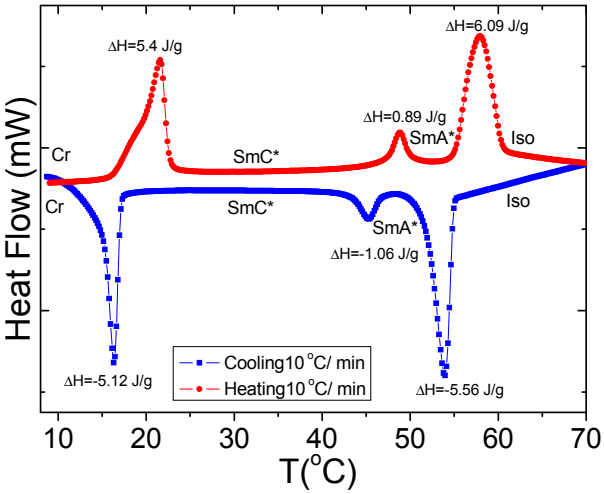

(**c**)

FIG. 2 (color online) (**a**) Molecular structure of the LC material MSi_3MR11, phase sequences and the transition temperatures (ºC) with enthalpies (J/g, in square brackets). (**b**) Optimized molecular geometry of MSi_3MR11. The arrow in Fig. 1b shows the direction of the molecular dipole moment (3.562 D).(**c**) DSC cooling and heating curves obtained at the rate of 10 ºC min^{-1}. The transition temperatures are obtained from the cooling cycle under the quasi-equilibrium condition at a rate of ~1 °C min^{-1} using polarizing microscopy. Iso=isotropic state, Cr= crystalline state.

The optimized geometry of MSi_3MR11 (shown in Fig. 2b) is obtained by Density Functional Theory (DFT) using B3LYP method with a 6-31G (d,p) level basis set. Optimized geometry computations were carried out using Gaussian 09 software package [24]. The DSC thermograms obtained for MSi_3MR11 are shown in Fig. 2c. In both heating and cooling cycles, this material exhibits three transition peaks. The peaks in the DSC correspond to the phase transitions I - SmA*, SmA* - SmC* and the crystalline state. These phases are additionally characterized by polarizing optical microscopy. During the cooling cycle, enthalpy of the phase transition Iso-SmA* is -5.56 J/g, whereas that of SmA*-SmC* is -1.06 J/g. The enthalpies associated with the transition temperatures (first cooling and second heating rates of 10 ºC min^{-1}) show that the SmA*-SmC* phase transition is weakly of the first order [8,25].

The representative optical textures in the SmA* and SmC* phases (Fig. 3) were recorded using the polarizing optical microscope (Olympus BX51) equipped with a CCD camera (SPOT, Diagnostic Instruments, Inc.) on a non-oriented sample prepared between a glass slide and cover slip placed in a Mettler Hotstage (FP82HT) with a thermal stability of ± 0.1°C.

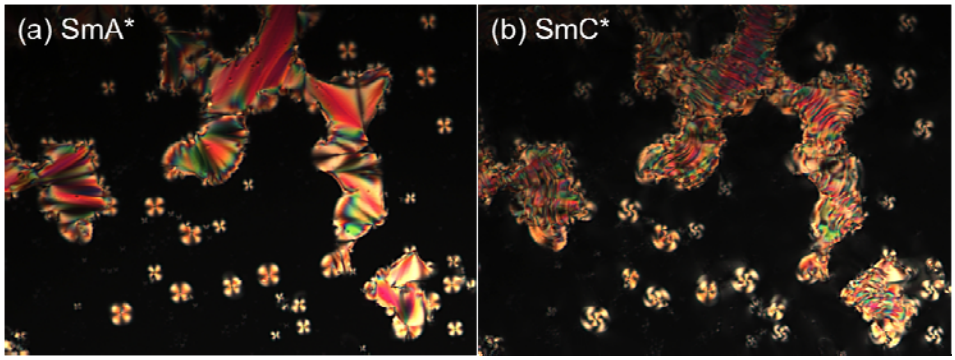

FIG. 3 (color online**)** Optical textures of MSi3MR11 in (**a**) SmA*, 5 ^{o}C above the SmA-SmC* transition, T_{AC}, and (**b**) SmC* (0.4 ^{o}C below T_{AC}), phases. The dark regions in the texture correspond to homeotropically aligned LC molecules.

The x-ray diffraction was studied on a sample contained in a flame sealed 1.0 mm quartz capillary and placed inside a Linkam hotstage (HFSX350-CAP) with 0.05 °C precision

temperature controller (T95-HS) for a definitive identification of the smectic phases and for temperature dependence studies of the structure parameters such as the layer spacing, tilt angle and the orientational order parameters. The x-ray diffraction measurements were performed using a microfocus Rigaku Screen Machine (Copper anode, λ = 1.542 Å) and the diffraction patterns recorded by Mercury 3 CCD detector of resolution 1024 × 1024 pixels (size: 73.2 × 73.2 μm^2) placed ~73 mm from the sample. The data was calibrated against silver behenate standards traceable to the National Institute of Standards and Technology. Data analyses were carried out using FIT2D software [26] and Mathematica on the background corrected data (*i.e.* scattering from an empty capillary was subtracted from the measured scattering data).

Electro-optic studies were made on planar cells filled with the material under study. The planar alignment in this cell is achieved by coating the indium tin oxide glass substrates with a RN1175 polymer alignment layer (Nissan Chemicals Japan) and baking the substrates at a temperature of 250 ^{o}C for 30 minutes. The gap between the substrates is controlled by Mylar spacers and the actual cell thickness is measured by the technique based on the optical interference of reflected beams of light from the inner faces of the substrates of the cell. The phases are characterized by using a polarizing optical microscope (Olympus BX 52) fitted with a hot stage connected to a temperature controller (Eurotherm 2604). The electro-optic behavior of the different phases is investigated by applying AC voltages of different amplitudes from a signal generator (Agilent 33120A) amplified by a high voltage amplifier (TReK PZD700). Dielectric spectroscopy over a frequency varying from 1 Hz-10 MHz is carried out using a broadband Alpha High Resolution Dielectric Analyzer (Novocontrol GmbH, Germany) under the application of a weak electric field of (0.1 V_{rms}) applied across the cell with brass electrodes.Temperature of the LC sample filled in the cell of gold coated brass electrodes is stabilized to ± 0.05 °C. The dielectric spectra are recorded during the cooling process from the isotropic state.

3. RESULTS AND DISCUSSIONS

3.1 The Free-standing film thickness and Birefringence measurements

The temperature dependence of the thickness of a free-standing film (FSF) is studied using a high-resolution interferometric measurement technique [27]. A good quality homeotropic alignment of LC molecules is achieved in the FSF of MSi_3MR11, the layer thickness covers ~10,000 layers. An experimental measurement is carried out by shining an unpolarized beam of light along the layer normal. Both heating and cooling cycles of the sample were carried

out with rates as low as 0.01°C/ min in order to avoid the change in the thickness that would occur by a possible destruction of a few layers of the sample when the heating/cooling rates were large enough. Figure 4 shows temperature dependence of the optical film thickness normalized to the thickness at the SmA-SmC phase transition for the compound under study. The optical film thickness is defined as its mechanical thickness multiplied by its effective refractive index. The thickness is measured with a high resolution interferometric technique to an accuracy better than 0.01%. If one simulates the refractive index with a change in the tilt angle, then the normalized or the relative layer thickness can be obtained. Below the isotropic temperature, the film thickness initially increases linearly but with a reduction in temperature [28] and on approaching the smectic A* - SmC* transition, the film thickness reverses its trend from increasing to decreasing with a reduction in temperature due to an onset of the tilt. This trend characterizes SmA* - SmC* transition. For ($T-T_{AC}$) varying from zero to - 0.61 ^{o}C, as seen in Fig. 4, a change in the normalized film thickness shows a sharp decrease with a large drop-off in thickness. This anomalous drop is the characteristic evidence for the first order SmA* - SmC* phase transition, labelled in Fig. 4 as the region where SmA* and SmC* coexist. If all the layers in this narrow temperature range were to be in the SmC* alone, the optical film thickness would have exhibited rather a linear low slope drop-off with temperature; contrary to what is observed here. As already stated, the first-order behavior is additionally corroborated by the DSC observations at the SmA* to SmC* transition (Fig. 2b), which shows it to be a weak first-order transition. On further cooling the film in the SmC* phase, its thickness continues to decrease only relatively slightly due to an increase in the tilt angle. Finally the layer thickness reaches $d_C \approx 0.9925 d_{AC}$ at 6.3 ºC below T_{AC}. In this material, the layer shrinkage of 0.75% is found to be close to the reported values of 0.73% and 0.65% for the other known de-Vries materials: W599 [21] and TSiKN65 [20], respectively. This small layer shrinkage is due to an increase in the tilt angle with a reduction in temperature; it is small because in going from SmA* to SmC*, the in-layer directors with azimuthal angles degenerated and distributed on to a cone in SmA* condense on to the azimuthal angles lying within narrower limits of the tilt in the SmC* phase (see Fig. 1b); this process on its own requires no change in the layer thickness.

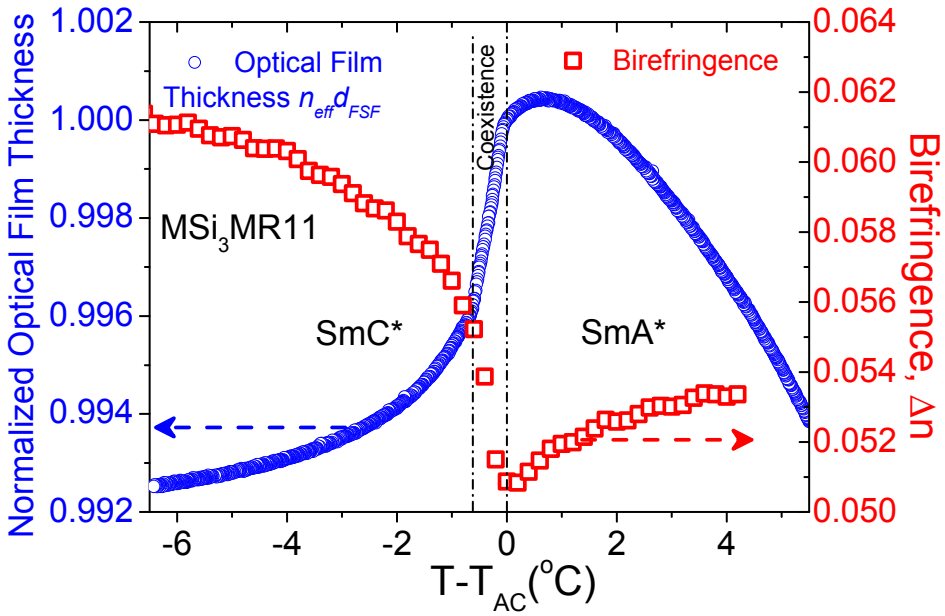

FIG. 4: (color online) Temperature dependence of the normalized optical film thickness; plotted as circles (□). Birefringence as squares, □, plotted as a function of temperature on the right-hand side of Fig. 4. Measurements of the birefringence are carried out in the absence of external field on a 3 μm planar cell under cooling from the isotropic state. The coexistence region shown by two vertical dotted lines, where the two phases co-exist, is the signature of the first-order phase SmA* - SmC* phase transition. In this narrow temperature range, if all the layers were to be in the SmC* alone, the optical film thickness would have shown a small linear drop-off with temperature.

Figure 4 also shows the plots of the apparent birefringence Δn and the optical layer thickness as a function of $(T\text{-}T_{AC})$.The magnitude of Δn first decreases on cooling and then starts to increase after the SmA* - SmC* phase transition has occurred [29]. The decrease in Δn is due to the de-Vries tilt appearing in the SmA* phase where the in-layer directors are distributed on the cone. Values of the birefringence, Δn, and the apparent optical tilt angle, θ_{App}, are determined by recording the transmitted beam of light through the LC sample where a set of crossed polarizer and analyzer is rotated using a procedure similar to that described by Park et al. [30]. Experiments were conducted by applying a triangular signal of frequency 46 Hz and an amplitude of 16 $V_{0\text{-}pk}/\mu m$. The frequency is so chosen as to allow sufficient time for switching to occur while avoiding the ionic conductivity from contributing to the switching current, and different from the mains frequency of 50 Hz to avoid interference from electrical noise to the output signal. Amplitude of the voltage applied should be large enough to saturate the tilt angle but at the same time it should be such be much lower than the dielectric breakdown of the sample by the electric field.

The field-induced tilt angle θ_{App} and Δn values for selected temperatures close to the SmA* - SmC* transition are plotted as a function of the applied field in Fig. 5. Magnitude of Δn increases with electric field (Fig. 5a) due to the lifting of degeneracy in azimuthal angle with the field. The behavior is typical of the diffuse-cone class of models for the SmA* phase. The tilt angle increases by the conventional electroclinic effect first and then finally it gets saturated with the field. This saturation in the tilt angle occurs in both SmC* and in the temperature range of SmA* closer to the SmA*-SmC* transition. At higher temperatures in the SmA* phase, the electroclinic effect itself is small and hence the electric fields applied are not large enough for the saturation in θ_{App} to show up; here θ_{App} shows almost linear response to the applied electric field [31] up to the value of θ_{App} ~ 15º. For temperatures closer to the SmC* - SmA* transition temperature, θ_{App} slightly deviates from the linear dependence on moderate values of the field, thus having a positive value of the second derivative with field. For large values of the electric field, θ_{App} continues to grow slowly and its second derivative becomes negative. Since the sigmoidal response of $\theta_{App}(E)$ and $\Delta n(E)$ could not be satisfactorily explained by Fukuda's Langevin-Debye approach [32], Shen et al. [21] proposed a modified model where they added additional term involving square of the electric field in the expression for the free energy.

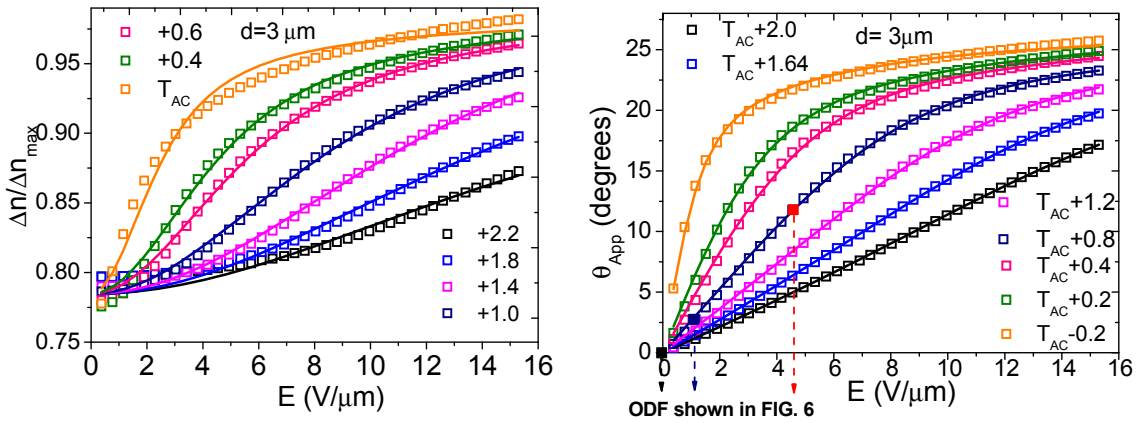

5(a) **5(b)**

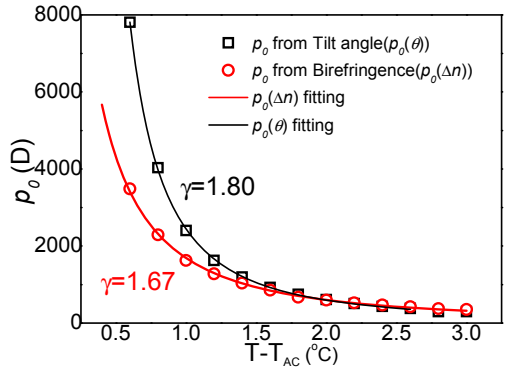

5(c)

FIG. 5: (color online) (**a**) Measured values of the birefringence as a function of the electric field are fitted to the generalized Langevin-Debye model (solid lines) [21], (**b**) the field induced optical tilt (experimental values in symbols) are fitted to this model (solid lines). Data points for the Orientational distribution function (ODF) to be shown in Fig. 6 are marked in Fig. 5b. (**c**) The local dipole moment p_0 obtained from (Δn and θ_{App} fits) as a function of the reduced temperature. The solid lines are the best fits to the power law equation for the total dipole moment $p_0(T) = A/(T-T_{AC})^{\gamma}$; γ is the power law exponent.

Inspite of the several approaches [32-36] that exist for modeling the unusual electro-optic characteristics of the de-Vries compounds; we choose the generalized Langevin-Debye model that was recently proposed by Shen et al. [21] for the better analysis of our data for the reasons given above. Fit of the data to the model leads to the orientational distribution function (ODF), with a complete azimuthal degree of freedom but the tilt θ is allowed to vary by the applied field within a certain range of values. A quadratic term in the electric field in the expression of free energy has been found to have significantly improved the fit of the experimental data to the model. According to this model the free energy, U, is expressed as:

$$U = -\boldsymbol{p}\left(1 + \alpha\frac{\boldsymbol{p}}{|\boldsymbol{P}|}\cdot\boldsymbol{E}\right)\cdot\boldsymbol{E} = -p_0 E\sin\theta\ \cos\varphi\ (1 + \alpha E\cos\varphi) \qquad (1)$$

Here $p = p_0\, sin\theta$ is the dipole moment of the domain correlated in the tilt brought about by the condensation of the azimuthal angle. The first term $(-p_0\, Esin\theta\, cos\varphi)$ given in Eqn. 1 describes the dipole interaction energy and the second term $(-p_0 E^2 sin\theta cos^2\varphi)$ includes the tilt susceptibility that increases with the square of the electric field. This term leads to the sigmoidal response in both Δn and θ_{App} with applied field. α is the phenomenological scaling factor. The tilt angle θ_{App} and the birefringence Δn as functions of the applied field become:

$$\tan 2\theta_{App} = \frac{\langle \sin 2\theta \cos\varphi\rangle}{\langle \cos^2\theta - \sin^2\theta\cos^2\varphi\rangle} \qquad (2)$$

$$\frac{\Delta n}{\Delta n_{max}} = \frac{\langle \cos^2\theta - \sin^2\theta\cos^2\varphi \rangle}{\cos 2\theta_{App}} \quad (3)$$

An average $\langle Y \rangle$ is estimated over the orientational distribution of molecules according to the formula $\langle Y \rangle = \int_{\theta_{min}}^{\theta_{max}} \int_0^{2\pi} Y(\theta,\varphi) f(\theta,\varphi) \sin\theta d\theta d\varphi$, where the mean field orientational distribution function $f(\theta,\varphi)$ is expressed as $f(\theta,\varphi) = exp[-U/k_B T] / \int_{\theta_{min}}^{\theta_{max}} \int_0^{2\pi} exp[-U/kBT] \sin\theta d\theta d\varphi$ [21]. In this model, the field induced angle varies between the values inferred from the birefringence at zero electric field (θ_{min}) to the maximum field (θ_{max}). For the latter Δn is assumed to be saturated by the field. Here, for MSi3MR11, the limiting values of the induced angle are found to be θ_{min} =16.93º and θ_{max} =26.63º (Fig. 5a, b). These limiting values of θ themselves are temperature independent but the actual value within these limits is nevertheless temperature dependent. Datasets obtained for both $\Delta n(E)$ and $\theta_{App}(E)$ are fitted by the model [21]. However in contrast to the procedure used in [21], the fitting is carried out separately for both $\Delta n(E)$ and $\theta_{App}(E)$. Though better fits for both (a) and (b) are obtained, however the fits with different power law exponents do reveal short-comings of the model. However both exponents are in the "de Vries - range" and outcome of the ODF is clearly "diffused-cone". If such a limation is material independent then this issue needs to be addressed in future.

Figure 6 shows the 'orientation distribution function' (ODF), $f(\theta,\varphi)$, for MSi_3MR11 at a temperature of T= (T_{AC}+0.8) ^oC for different strengths of the electric field. The simulated ODF is rather close to a corresponding result demonstrated earlier for a different material (Fig. 5 (a,b) in ref [21]). One can see that the model enforces a clear diffused cone distribution – by confining the cone angle between the limits of θ_{min} and θ_{max}. In this case, the re-distribution of the azimuthal angles of molecules caused by the electric field generates a finite apparent optical tilt angle very close to the one found in the experiment (Fig. 5b). For the higher field strengths, nearly all of the molecules are aligned along a single direction on the outer (θ_{max}) cone. Note that the modelled ODF shown in Fig. 6 corresponds to the aromatic core part of the molecule that exhibits birefringence in the visible range of wavelengths.

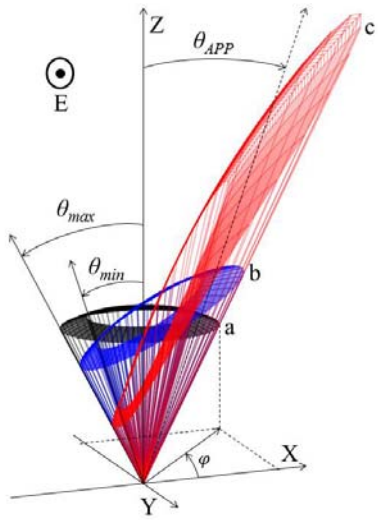

FIG. 6 (color online): The Orientation Distribution Function $f(\theta, \varphi)$ of MSi_3MR11 at a temperature of $T = (T_{AC} + 0.8)$ ^oC for various values of electric field strengths – (a) 0 V/µm (black); (b) 1.14 V/µm (blue); and (c) 4.17 V/µm (red). *X*-*Y* is the smectic layer plane and *Z* is directed along the layer normal. Electric field is applied along the *Y* direction which lies in the smectic layer.

The local dipole moment p_0, (Fig. 5c), determined as a fitting parameter increases with decreasing temperature in the SmA* phase. On approaching the SmA* - SmC* transition from the high temperature side, the magnitude of p_0 in the generalized Langevin-Debye model diverges corresponding to the correlation length of the tilt domain where the azimuthal angle is condensed to values within narrow limits. Here the magnitudes of p_0 obtained from the fitting of the birefringence and the tilt data are somewhat different in the vicinity of the smectic SmA* - SmC* transition. Also, the scaling parameter α of the electric field varies from 0.017 to 0.023 µm/V for birefringence and ~ 0.024 to 0.11 for data on the tilt angle. This clearly indicates that the system is more complex than the simple assumptions made in this model despite the quality of the individual fits of Δn and the apparent tilt angle to the model. One of the main reasons for this discrepancy could be that the model assumes constant values of θ_{min} and θ_{max} independent of temperature. But measurements on the layer thickness and on temperature dependence of the zero-field birefringence reveal that θ_{min} does at least vary with temperature. The second reason could be that the molecular biaxiality that is neglected in the model so far has to be taken into account [33].

To analyze the temperature dependence of the correlated dipole moment, p_0, we fit the data to the power law equation, $p_0(T) = A/(T-T_{AC})^{\gamma}$ (Fig. 5c), γ is the power law exponent. The fit is found to be excellent but temperature dependencies of the local dipole moment are

different for the birefringence and the apparent tilt angle. Exponents for and are found to be 1.67 and 1.80, respectively. These fits lead to the conclusion that the correlated tilt (or the correlation length) increases with a reduction in temperature in the SmA* phase [37], this is reminiscent of the de-Vries behavior [9,18].

3.2 X-ray Diffraction

The x-ray diffraction pattern for the SmA* shows sharp Bragg layer reflection peaks in the small angle region centered at ~39.6 Å and the 2nd order reflection centred at ~19.8 Å, shown in Fig. 7a. A pair of diffuse crescents in the wide-angle region perpendicular to the layer peak located at ~4.6 Å confirm the orthogonal smectic (SmA) nature of this phase. In the SmC* phase (Fig. 7b), the 3rd order smectic reflections appear at ~13.4 Å and the crescents are centered at 4.6 Å perpendicular to the layer peaks, this seems to be indistinguishable from the SmA* phase. However, the pair of wide-angle crescents are more diffuse in the SmC* phase, than in SmA*, where each crescent can be approximated as a sum of the two crescents separated by an angle 2α, α being the molecular tilt angle with respect to the layer normal. This corresponds to the domain structure with the opposite tilts, as illustrated in the inset of Fig. 7b.

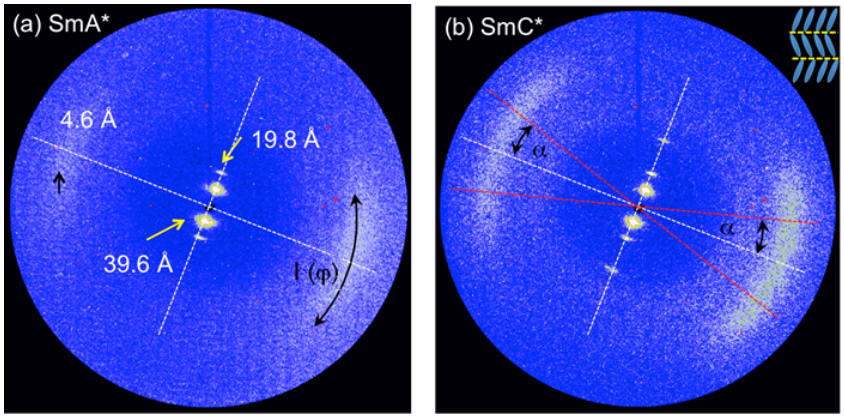

Fig. 7: Representative x-ray diffractions patterns of MSi3MR11 in **(a)** SmA* phase (1.2 °C above the T_{AC}) and **(b)** SmC* phase (17.5 °C below the T_{AC}). Inset of (**b**) depicts the SmC* structure.

The temperature dependence of the smectic layer spacing (Fig. 8a), determined from the Lorentzian fits to the first small-angle peak reveals 1.75% maximum layer shrinkage in the SmC* phase, approximately 20 degrees below the smectic A* to C* transition. Note that the optical layershrinkage of 0.75% mentioned above is based on the smallest d_C spacing, obtained approximately 6 degrees below the smectic AC transition. The inset in Fig. 8a shows a comparison between the layer thickness measured by x-ray with the optical FSF thickness, the

latter is normalized by the value at the SmA* to SmC* transition temperature. A different trend in between the two is due to a change in the refractive index tensor by the molecular tilt angle θ [27]. On cooling the cell in SmC* this deviation reaches ~20% of the total shrinkage which can be explained by a larger value of the tilt at the phase transition point as compared to the material described in [27]. The tilt angle, α in the SmC* phase was calculated as half the angle of separation between the centers of the two Gaussian fits to the azimuthal intensity distribution, $I(\varphi)$ of the wide angle reflection at 4.6 Å, Fig. 8b. Owing to the difficulty in obtaining a single domain sample, a reasonable temperature dependence of the tilt angle in the SmC* phase specifically close to the SmA* - SmC* transition was difficult to determine. Nonetheless, the maximum calculated tilt angle α_{max} is ~20° in the lower SmC* phase.

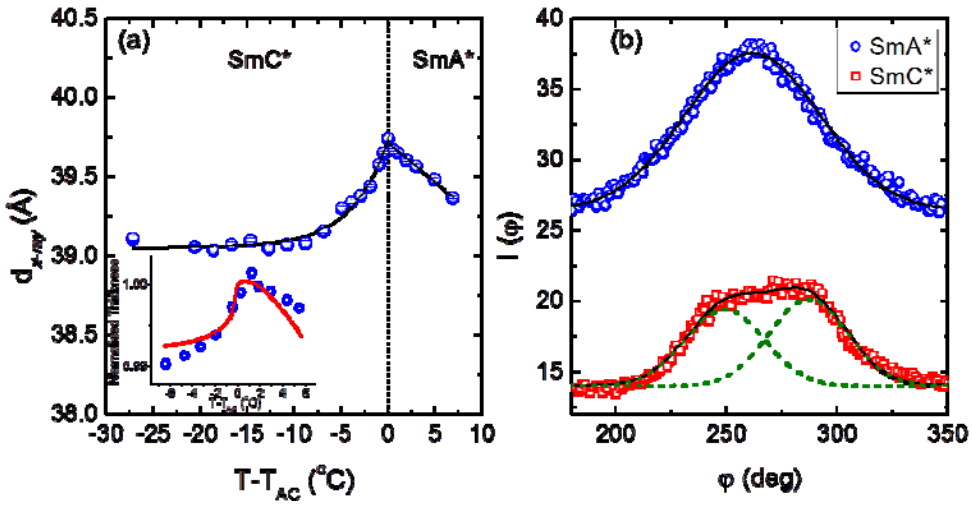

(**a**) (**b**)

FIG. 8. (color online): (**a**) Temperature dependence of the layer spacing determined from the x-ray diffraction. A comparison of the results of the layer thickness from the free standing film experiment (red solid line) and the layer thickness from the x-ray results as discrete points (circles) given in the inset. Both curves in the inset are normalized (**b**) The representative azimuthal intensity distribution $I(\varphi)$ of the wide-angle reflection centered at 4.6 Å in the SmA* (open circles) and in the SmC* (open squares) phases. The solid black line in SmA* is a single Gaussian fit (FWHM=64), while in SmC*, it is the sum of two Gaussian fits (dashed-lines) with FWHM = 36.

The orientational order parameter, $\langle P_2(\cos\beta)\rangle$ from the azimuthal intensity distribution $I(\varphi)$ of the wide angle reflection centered at ~ 4.6 Å (Fig. 7b) is determined using the method of Davidson et al. [38], numerical inversion method increased the value from 0.41± 0.01 (SmA*) to 0.58 ±0.01 (SmC*). Here, β corresponds to the angle between the director and the long axis of the molecule. The low values of $\langle P_2\rangle$ obtained here are the typical ones for the de-Vries compounds with chiral components, as compared to the $\langle P_2\rangle$ for de-Vries without chiral components [12,13], however these low values are also partly attributed to the presence of multi

domains in the scanned sample volume. Correspondingly, the average molecular fluctuation [13] ⟨β⟩, decreased from 35.8°± 0.2 (SmA*) to 31.6° ± 0.2 (SmC*). The extent of molecular fluctuations in SmA* is much larger than the measured maximum apparent tilt, θ_{App}~ 25° which obscures the dip in the expected volcano-shaped ODF for de-Vries compounds and effectively appears as sugarloaf distribution shown in Fig. 9 as a solid line. To illustrate this, a simulated orientational distribution function ODF with respect to the layer normal in de-Vries SmA phase with a polar tilt angle α = 25° and the molecular fluctuations ⟨β⟩ ~23° is also shown in Fig. 9 (red dashed line). Note that the x-ray diffraction probes the electron density related to the overall molecular length, thus the sugarloaf-shaped ODF obtained from the x-ray experiment does not rule out the diffuse-cone distribution obtained from the visible light optical parameters of the same compound.

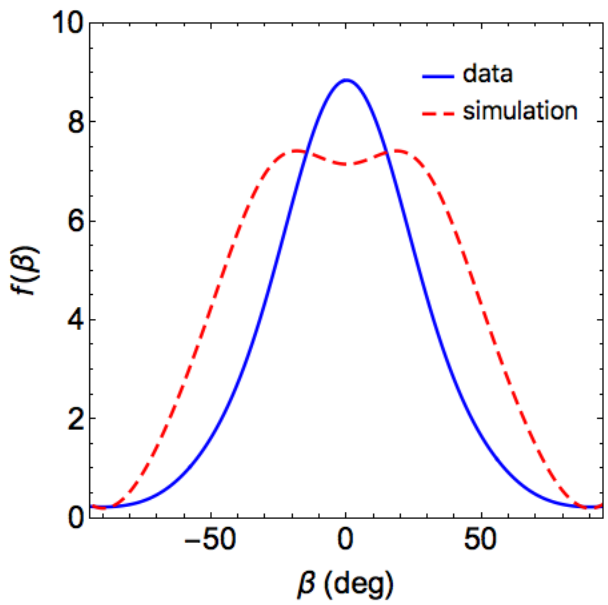

FIG. 9. (color online) The orientational distribution functions in the SmA* phase determined from the experimentally measured *I(φ)* (solid line) and the simulation (red dashed line).using molecular fluctuations ⟨β⟩ = 23° and the tilt angle α = 25°

3.3 Spontaneous Polarization Measurement

The spontaneous polarization $\boldsymbol{P_S}$ is measured using a planar cell of thickness 4 μm as a function of temperature and the results are shown in Fig. 10. For conducting the experiment, an external triangular wave ac voltage of 50 $V_{pk\text{-}pk}$ of frequency 152 Hz is applied across the planarly aligned cell using the method reported previously [39]. Measured value of Ps corresponds to its saturated value by the external field at the temperature of interest . The LC under study gives $\boldsymbol{P_S}$ ~ 124 nC cm^{-2} for a temperatiure of T=(T_{AC} - 13.5) ^{o}C.

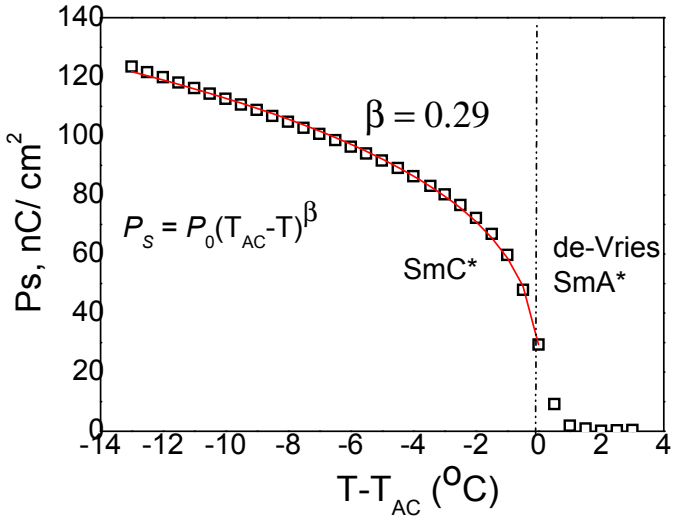

FIG. 10. (color online) Spontaneous polarization $\boldsymbol{P_S}$ *vs* ($T-T_{AC}$) measured on 4 μm planar cell under cooling from the isotropic state. A triangular-waveform voltage of 50 Vpk to pk at a frequency of 152 Hz is used in the experiment. $P_0 = 56.9$ nC. cm^{-2} .

Ps values are fitted to the power law equation $P_S = P_0\,(T_{AC} - T)^{\beta}$. In the fitting, it is not possible to include the values *Ps* in the SmA phase. The power law exponent, $\beta = 0.29$, is found from the fitting. This value so determined is close to that for the tricritical behavior; i.e. the point where the first and second order transitions meet with each other. The transition can then be described as 'a weakly first order transition'.

3.4 Dielectric Spectroscopy

Figure 11a shows the three dimensional plot of temperature dependent dielectric loss spectra (ε'') of a planarly-aligned cell filled with MSi_3MR11. The electrodes are made up of brass, these are gold-plated so as to have almost zero contact resistance. This is done to avoid the parasitic effects of the finite resistance of ITO electrodes acting in series with the cell-capacitance on the dielectric spectra.

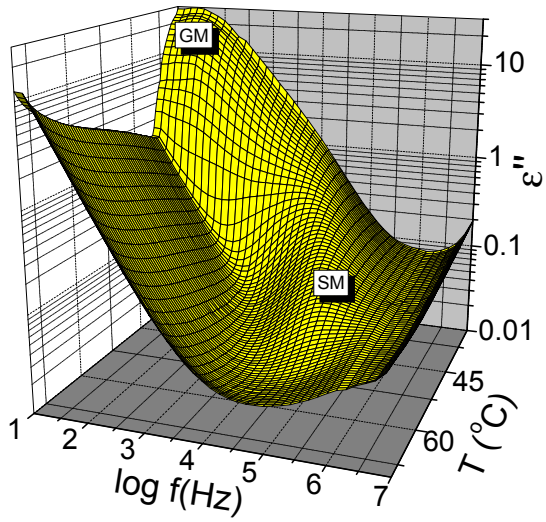

(**a**)

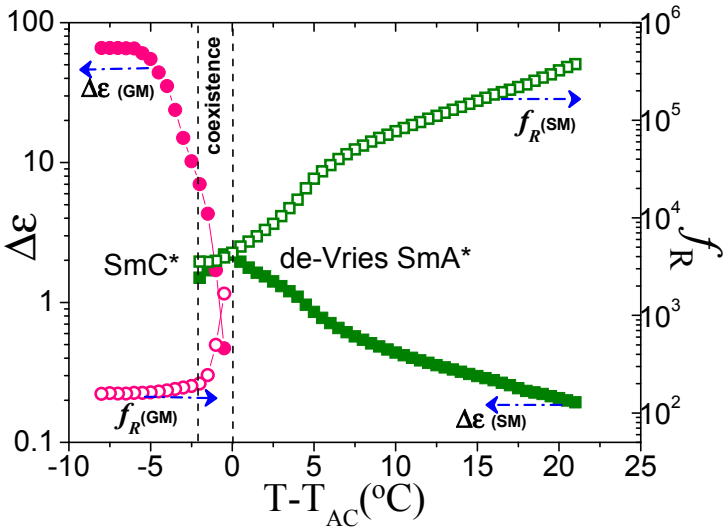

(b)

FIG. 11. (color online) (**a**) The three dimensional (3D) plot of temperature dependent dielectric loss spectra (ε'') for a 10 μm planarly aligned cell in the frequency range 1 Hz - 10 MHz. The dielectric measurements are carried out on the sample under cooling from the isotropic state. Temperature is stabilized to ± 0.05 ^{0}C and the applied voltage in the experiment is fixed as 0.1 V_{rms}. (**b**) The dielectric relaxation strength $\Delta\varepsilon$ and the relaxation frequency f_R for both the Goldstone (GM) and soft (SM) modes are plotted as a function of the reduced temperature. The temperature range where the two phases co-exist is shown by a set of vertical dotted lines close to the transition temperature.

The dielectric measurements are carried out over a frequency range of 1 Hz to 10 MHz using a broadband Alpha High resolution Dielectric analyser (Novocontrol GmbH, Germany), measurement made under a weak applied voltage of 0.1 V_{rms}. Temperature of the cell is controlled to within ± 0.05 ^{o}C. The temperature dependencies of the dielectric strength ($\Delta\varepsilon$) and

the relaxation frequency (f_R), are obtained by fitting the dielectric spectra to the Havriliak - Negami equation [40] :

$$\varepsilon^*(\omega) = \varepsilon' - i\varepsilon'' = \varepsilon_\infty + \sum_{j=1}^{n} \frac{\Delta\varepsilon_j}{\left[1 + \left(i\omega\tau_j\right)^{\alpha_j}\right]^{\beta_j}} - \frac{i\sigma_{dc}}{\varepsilon_0\omega} \tag{4}$$

Here, ε_∞ is the high frequency permittivity that includes the atomic and electronic polarizabilities, j is the number of relaxation processes and it varies from 1 to n, $\omega=2\pi f$ is the angular frequency, ε_0 is the permittivity of free space, $\Delta\varepsilon_j$ refers to the dielectric relaxation strength of the jth mode. α_j ($0 << \alpha_j \leq 1$) and β_j ($0 << \beta_j \leq 1$) are the symmetric and asymmetric broadening parameters of the complex dielectric function of the jth relaxation process. The $\sigma_{dc}/\varepsilon_0\omega$ is contribution of the dc conductivity to ε''. The relaxation frequency, f_j, of the jth relaxation process is related to its relaxation time τ_j as [41]:

$$f_j = \frac{1}{2\pi\tau_j}\left[\frac{\sin(\alpha_j\pi)}{2+2\beta_j}\right]^{1/\alpha_j}\left[\frac{\sin(\alpha_j\beta_j\pi)}{2+2\beta_j}\right]^{-1/\alpha_j} \tag{5}$$

In this case we fix $j = 2$ as we focus on to the two predominant modes: Goldstone mode (GM) and the soft mode (SM) over a restricted range of frequencies; inspite of the fact that many additional modes can possibly exist in a FLC cell [42]. The dielectric spectra are analysed using WINFIT programme purchased from Novocontrol GmbH. Temperature dependencis of the dielectric strength ($\Delta\varepsilon$) and relaxation frequency (f_R) for the two modes are shown in Fig. 11b. On cooling the cell from the isotropic state, the amplitude of the $\Delta\varepsilon$ increases and reaches a maximum value at the SmA* - SmC* phase transition. The corresponding f_R decreases on cooling over a broad temperature range of SmA* phase but with a sharper trend in its lower temperature range. In the studied chiral MSi3MR11 material, the soft mode fluctuation is dielectrically active in the SmA* phase due to the component of the dipole moment parallel to the probe field fluctuating with the applied electric field. Remarkably strong soft mode absorption is found in the dielectric spectra of de-Vries materials over a broader temperature range in comparison to the materials that exhibit a conventional SmA phase. For example the dielectric strength rises continuously with a reduction in temperature in this sample as opposed to a sudden rise of $\Delta\varepsilon$ in a conventional SmA phase, [compare Fig. 11b with Fig. 1b of Ref. 43] and Fig. 11b with Fig. 8a and 8b of [44]. Similarly the soft-mode relaxation frequency continuously decreases over a very wide temperature range in SmA* in this sample as opposed to conventional SmA in which a sudden change in the frequency occurs over a very narrow

range of temperatures close to the SmA* - SmC* transition [compare Fig. 11b with Fig 1b of [43]] for the relaxation frequency.

4. CONCLUSIONS

The siloxane liquid crystalline compound exhibiting de-Vries SmA* phase was studied by DSC, polarizing optical microscopy, XRD, FSF, electro-optics and dielectric spectroscopy. MSi_3MR11 shows a direct transition to SmA* phase on cooling from the isotropic state. Calorimetric studies confirm earlier works on the LC thermograms that report first order SmA*-SmC* phase transition in de-Vries LCs. Based on the results of Δn and θ_{App} measurements, together with the minimum layer shrinkage (~1.75%) obtained in this case, we characterize SmA* of the studied material to be of the de-Vries type, since an increase in the tilt angle with reducing temperature leads to decrease in magnitude of the birefringence. An increasing Δn with applied field was found in the vicinity of SmA*-SmC* transition. The generalised Langevin-Debye model as proposed by Shen et al. [21] is used to explain the electro-optical effects observed experimentally in the de-Vries SmA* phase of this material. While retaining power law dependencies of the optical parameters (Δn, θ_{App}) on temperature with slightly different exponents, the observed phenomena are well described by this model. The critical exponents indicate that dimension of the system is greater than unity in agreement with the de-Vries nature of the material. The soft mode relaxation strength from dielectric spectroscopy shows a critical behavior when the LC system approaches SmA* to SmC* phase transition. The future development of the de-Vries model should include temperature dependencies of the minima and maxima of cone angles and the molecular biaxiality must be included in the model parameters. X-ray scattering gives rise to sugar-loaf orientational distribution function but it does not exclude the observation of the diffused cone model for the electro-optical effects (birefringence and the tilt angle) as explained in the text. It would also appear that the presence of the two chiral centres in the molecule does not prevent this material from exhibiting the de Vries behaviour.

ACKNOWLEDGEMENTS

This work was supported by 13/US/I2866 from the Science Foundation of Ireland as part of the US–Ireland Research and Development Partnership program jointly administered with the United States National Science Foundation under grant number NSF-DMR-1410649 and by the DFG (Grant TS 39/24-1). A. Kocot thanks National Science Centre Poland for grant 2011/03/B/ST3/03369.

493 **Appendix A:**

494 **Synthetic Procedure**

495 All reagents were purchased from Sigma Aldrich, Fluorochem, Alfa Aesar, ABCR and used
496 without any further purification. Solvents were purchased from Sigma Aldrich, DMF was
497 purchased pre-dried, THF was dried using a sodium/benzophenone still under N_2. All reactions
498 were generally carried out under argon using oven-dried glassware. TLC plates were performed
499 on Merck silica gel 60 F_{254} and were visualized using a 254 nm light source. Flash column
500 chromatography was performed on Fluorochem silica gel 60 (40-63 micron).

501 ^{1}H and ^{13}C spectra were recorded at 25°C ($CDCl_3$ as solvent and TMS as reference) using a
502 Bruker 400 MHz Ultrashield (Avance 400). HRMS spectra were recorded using a Waters – TOF
503 Electrospray micromass LCT premier.

504 Procedures for each reaction are provided below.

505

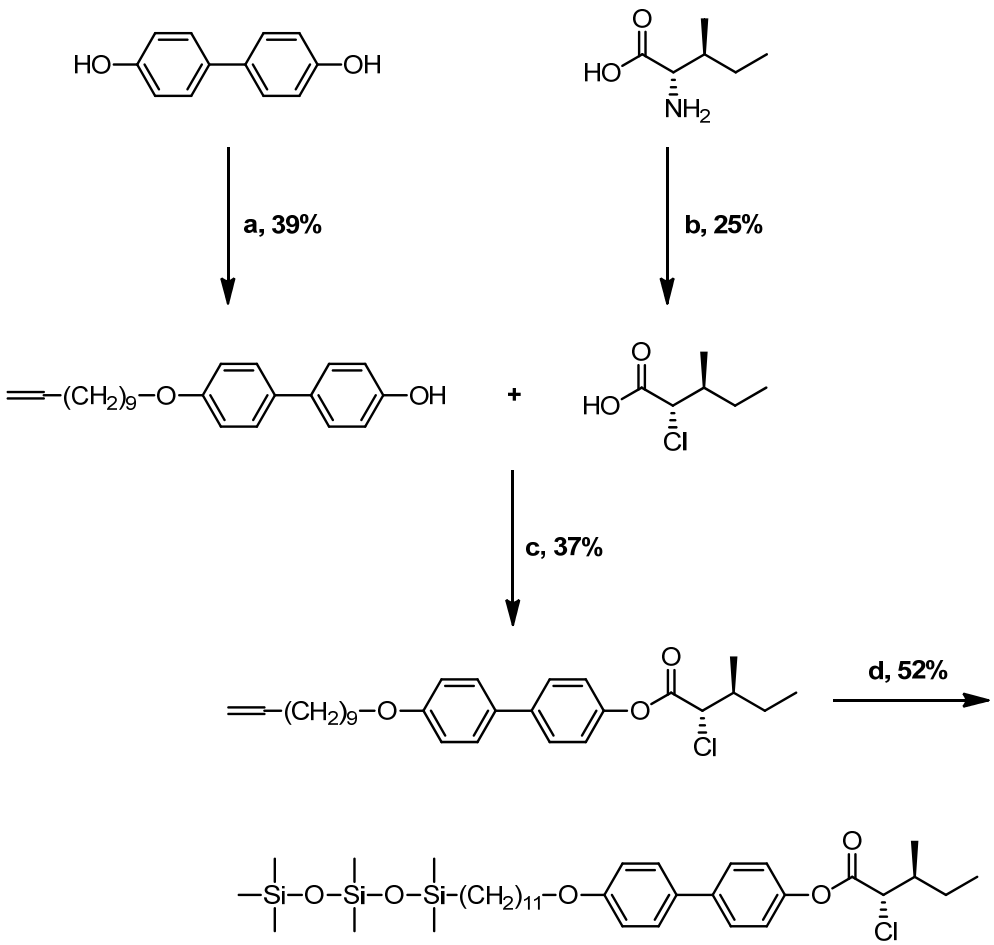

506

507 **Fig. 12**. Reagents and conditions: a) 11-bromo-1-undecene, K_2CO_3, DMF; b) $NaNO_2$, HCl, H_2O,
508 0 ^{o}C; c) DMAP, DCC, THF; d) 1,1,1,3,3,5,5-heptamethyltrisiloxane, Karstedt's catalyst, THF.

509

510

511 4'-(undec-10-en-1-yloxy)-[1,1'-biphenyl]-4-ol (**T1**)

512 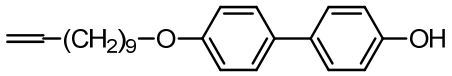

513

514 **FIG. 13, T1**

515

516 4,4′-dihydroxybiphenyl (5.00 g, 26.85 mmol), 11-bromo-1-undecene (6.26 g, 26.85 mmol) and
517 potassium carbonate (3.72 g, 26.92 mmol) were dissolved in dry DMF (25 mL) under nitrogen
518 and stirred at room temperature overnight. Water (25 mL) was added, the solution was
519 neutralised with HCl (1M) and the precipitate was filtered. The solid was dissolved in hot
520 ethanol and any insoluble particles were filtered. The suspension which formed is then filtered a
521 second time to yield a white powder (3.40 g, 10.04 mmol, 37%).

522 ^{1}H NMR (400 MHz, $CDCl_3$) δ: 7.45 (d, J = 6.7, 2H), 7.42 (d, J = 6.6, 2H), 6.94 (d, J = 8.7, 2H),
523 6.88 (d, J = 8.6, 2H), 5.82 (m, 1H), 4.98 (m, 2H), 4.72 (m, 1H), 3.98 (t, J = 6.6, 2H), 2.04 (m,
524 2H), 1.78 (m, 2H), 1.65-1.2 (m, 12H).

525 (2S,3S)-2-chloro-3-methylpentanoic acid (**T2**)

526 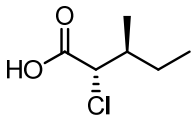

527 **FIG. 14, T2**

528 A suspension of L-isoleucine (5.00 g, 38.12 mmol) in 6M HCl (40 mL) was cooled to 0 ^{o}C. A
529 solution of sodium nitrite (2.63 g, 38.12 mmol) in water (15 mL) was added drop-wise. Solution
530 was stirred for 4 hours at 0 ^{o}C and 1 hour at room temperature. The compound was extracted
531 with ethyl acetate and dried with magnesium sulphate. The solvent was evaporated and the oil
532 distilled to give a light yellow oil (1.43 g, 9.50 mmol, 25%).

533 ^{1}H NMR (400 MHz, $CDCl_3$) δ: 9.28 (s, 1H), 4.22 (d, J = 6.5, 1H), 2.10 (m, 1H), 1.65 (m, 1H),
534 1.34 (m, 1H), 1.05 (d, J = 6.8, 3H), 0.92 (t, J = 7.4, 3H).

535 (2S,3S)-4'-(undec-10-en-1-yloxy)-[1,1'-biphenyl]-4-yl 2-chloro-3-methylpentanoate T3

536

537

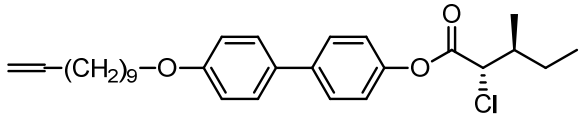

(FIG. 15, T3)

A solution of T1 (1.00 g, 2.95 mmol), T2 (0.44 g, 2.95 mmol), DMAP (0.04 g, 0.33 mmol) and N,N'- Dicyclohexylcarbodiimide (0.61 g, 2.96 mmol) in dry THF (30 mL) were sealed under nitrogen and stirred overnight at room temperature. The precipitate was filtered and solvent evaporated. Crude was purified using column chromatography (ethyl acetate/hexane, 1:1, R_f = 0.63). The compound was then dissolved in hot petroleum ether and any precipitate was filtered away to give a yellow wax (0.52 g, 1.10 mmol, 37%).

^{1}H NMR (400 MHz, $CDCl_3$) δ: 7.56 (d, *J* = 8.6, 2H), 7.48 (d, *J* = 8.7, 2H), 7.16 (d, *J* = 8.6, 2H), 6.96 (d, *J* = 8.7, 2H), 5.82 (m, 1H), 4.97 (m, 2H), 4.40 (d, *J* = 7.1, 1H), 3.99 (t, *J* = 6.5, 2H), 2.24 (m, 1H), 2.05 (m, 2H), 1.80 (m, 3H), 1.70-1.16 (m, 14H), 1.15 (d, *J* = 6.7, 3H), 1.00 (t, *J* = 7.4, 3H).

(2S,3S)-4'-((11-(1,1,3,3,5,5,5-heptamethyltrisiloxanyl)undecyl)oxy)-[1,1'-biphenyl]-4-yl 2-chloro-3-methylpentanoate MSi3-MR11

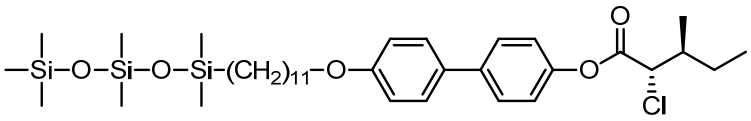

FIG. 16, MSi3-MR11

A solution of T3 (0.20 g, 0.42 mmol) in dry THF (10 mL) was put under nitrogen. 1,1,1,3,3,5,5-heptamethyltrisiloxane (0.14 g, 0.63 mmol) and platinum(0)-1,3-divinyl-1,1,3,3-tetramethyldisiloxane (0.021 mmol, 420 µL of 0.05 M solution) were added to the solution which was stirred for ~4 hours until the double bond was fully reduced. Solvent was evaporated and compound purified using column chromatography (DCM/Hexane, 2: 8, where R_f = 0.76 in ethyl acetate: hexane, 1:9), to give a white wax (0.15 g, 0.22 mmol, 52%).

^{1}H NMR (400 MHz, $CDCl_3$) δ: 7.55 (d, *J* = 8.8, 2H), 7.48 (d, *J* = 8.8, 2H), 7.16 (d, *J* = 8.8, 2H), 6.96 (d, *J* = 8.8, 2H), 4.39 (d, *J* = 7.1, 1H), 3.99 (t, *J* = 6.6, 2H), 2.23 (m, 1H), 1.80 (m, 3H), 1.52-1.22 (m, 17H), 1.15 (d, *J* = 6.8, 3H), 0.99 (t, *J* = 7.5, 3H), 0.53 (m, 2H), 0.09 (s, 9H), 0.06 (s, 6H), 0.02 (s, 6H).

^{13}C NMR (101 MHz, CDCl3) δ: 168.29 (C), 159.12 (C), 149.49 (C), 139.42 (C), 132.72 (C), 128.33 (CH), 128.00 (CH), 121.58 (CH), 115.07 (CH), 68.36 (CH2), 62.88 (CH), 39.31 (CH), 33.68 (CH2), 29.87 (CH2), 29.82 (2CH2), 29.64 (CH2), 29.62 (CH2), 29.52 (CH2), 26.29 (CH2), 25.39 (CH2), 23.45 (CH2), 18.52 (CH2), 16.22 (CH3), 11.11 (CH3), 2.04 (3CH3), 1.50 (2CH3), 0.43 (2CH3).

HRMS (EI): calcd for $C_{36}H_{61}ClO_5Si_3Na$ [M + Na^+] 715.3413, found: 715.3438.

REFERENCES

[1] S. Kumar, Phys. Rev. A **23**, 3207 (1981).

[2] C. R. Safinya, R. J. Birgeneau, J. D. Litster, and M. E. Neubert, Phys. Rev. Lett. **47**, 668 (1981).

[3] J. P. Lagerwall and F. Giesselmann, Chem. Phys. Chem. **7**, 20 (2006).

[4] T. P. Rieker, N. A. Clark, G. S. Smith, D. S. Parmar, E. B. Sirota, and C. R. Safinya, Phys. Rev. Lett. **59**, 2658 (1987).

[5] N. A. Clark and S. T. Lagerwall, Appl. Phys. Lett. **36**, 899 (1980).

[6] S. Diele, P. Brand, and H. Sackmann, Mol. Cryst. Liq. Cryst. **16**, 105 (1972).

[7] A. de Vries, Abstracts Book of the 5th International Liquid Crystal Conference, 150, Stockholm, (1974).

[8] A. de Vries, Mol. Cryst. Liq. Cryst. **41**, 27 (1977).

[9] A. de Vries, A. Ekachai, and N. Spielberg, Mol. Cryst. Liq. Cryst. Lett. **49**, 143 (1979).

[10] Y. Takanishi, Y. Ouchi, H. Takezoe, A. Fukuda, A. Mochizuki, M. Nakatsuka, Jpn. J. Appl. Phys. **29**, L984 (1990).

[11] M. D. Radcliffe, M. L. Brostrom, K. A. Epstein, A. G. Rappaport, B. N. Thomas, R. Shao, and N. A. Clark, Liq. Cryst. **26**, 789 (1999).

[12]. H. G. Yoon, D. M. Agra-Kooijman, K. Ayub, R. P. Lemieux, and S. Kumar, Phys. Rev. Lett. **106**, 087801 (2011).

[13] D. M. Agra-Kooijman, H. G. Yoon, S. Dey, and S. Kumar, Phys. Rev. E **89**, 032506 (2014).

[14] K. Merkel, A. Kocot, J. K. Vij, P. J. Stevenson, A. Panov, and D. Rodriguez, Appl. Phys. Lett. **108**, 243301 (2016).

[15] N. Hayashi, T. Kato, A. Fukuda, J. K. Vij, Yu. P. Panarin, J. Naciri, R. Shashidhar, S. Kawada and Sh. Kondoh, Phys. Rev. E **71**, 041705 (2005).

[16] Ch. Bahr and G. Heppke, Phys. Rev. A **41**, 4335 (1990).

[17] U. Manna, J. –K. Song, Yu. P. Panarin, A. Fukuda and J. K. Vij, Phys. Rev. E **77**, 041707 (2008).

[18] O. E. Panarina, Yu. P. Panarin, J. K. Vij, M. S. Spector, and R. Shashidhar, Phys. Rev. E **67**, 051709 (2003).

[19] O. E. Panarina, Yu. P. Panarin, F. Antonelli, M. Reihmann, and G. Galli, J. Mater. Chem. **16**, 842 (2006).

[20] M. S. Spector, P. A. Heiney, J. Naciri, B. T. Weslowski, D. B. Holt and R. Shashidhar, Phys. Rev. E **61**, 1579–1584 (2000).

[21] Y. Shen, L. Wang, R. Shao, T. Gong, C. Zhu, H. Yang, J. E. Maclennan, D. M. Walba, and N. A. Clark, Phys. Rev. E **88**, 062504 (2013).

[22] J. P. F. Lagerwall, F. Giesselmann and M. D. Radcliffe, Phys. Rev. E **66**, 031703 (2002).

[23] G. Galli, M. Reihmann, A. Crudeli, E. Chiellini, Yu. P. Panarin, J. K. Vij, C. Blanc, V. Lorman, and N. Olsson, Mol. Cryst. Liq. Cryst. **439**, 2111 (2005).

[24] M. J. Frisch et al.; Gaussian 09, Revision E.01 Gaussian, Inc., Wallingford CT, (2009).

[25] A. Mchisuki, and S. Kobayashi, Mol. Cryst. Liq. Cryst. **243**, 77 (1994).

[26] A. P. Hammersley, S. O. Svensson, M. Hanfland, A. N. Fitch, and D. Hausermann, High Pressure Research **14**, 235. 1996

[27] V. P. Panov, J.K. Vij, Yu. P. Panarin, C. Blanc, V. Lorman, J. W. Goodby, Phys. Rev. E **75**, 042701 (2007).

[28] K. L. Sandhya, Yu. P. Panarin, V. P. Panov, J. K. Vij and R. Dabrowski, Eur. Phys. J. E **27**, 397 (2008).

[29] K. Saunders, D. Hernandez, S. Pearson, and J. Toner, Phys. Rev. Lett. **98**, 197801 (2007).

[30] B. Park, S. -S. Seomun, M. Nakata, M. Takahashi, Jpn. J. Appl. Phys. **38**, 1474-1481 (1999).

[31] S. Garoff and R. B. Meyer, Phys. Rev. Lett. **38**, 848 (1977); Phys. Rev. A **19**, 338 (1979).

[32] A. Fukuda, Proceedings of the 15th International Display Research Conference of the SID (Society for Information Display, San Jose, California, 1995), p. 61; S. Inui, N. Iimura, T. Suzuki, H. Iwane, K. Miyachi, Y. Takanishi, and A. Fukuda, J. Mater. Chem. **6**, 671 (1996).

[33] J. V. Selinger, P. J. Collings, and R. Shashidhar, Phys. Rev. E **64**, 061705 (2001).

[34] N. A. Clark, T. Bellini, R. Shao, D. Coleman, S. Bardon, D. R. Link, J. E. Maclennan, X. Chen, M. D. Wand, D. M. Walba, P. Rudquist, and S. T. Lagerwall, Appl. Phys. Lett. **80**, 4097 (2002).

[35] P. J. Collings, B. R. Ratna, and R. Shashidhar, Phys. Rev. E **67**, 021705 (2003).

[36] Z. V. Kost-Smith, P. D. Beale, N. A. Clark, and M. A. Glaser, Phys. Rev. E **87**, 050502(R) (2013).

[37] P. G. de Gennes and J. Prost, The Physics of Liquid Crystals, 2nd ed. (Clarendon Press, Oxford, 1993), Sec. 10.2.1.

[38] P. Davidson, D. Petermann, and A. M. Levelut, J. Phys. II **5**, 113 (1995).

[39] V. M. Vaksman and Yu. P. Panarin, Molecular Materials, **1**, 147 (1992); V. Panov, J. K. Vij, and N. M. Shtykov, Liquid Crystals, **28**, 615 (2001).

[40] S. Havriliak (Jr.) and S. Negami, Polymer, **8**, 161 (1967).

[41] O. E. Kalinovskaya and J. K. Vij, J. Chem. Phys. **111**, 10979 (1999).

[42] Yu. P. Panarin, H. Xu, S. T. Mac Lughadha, and J. K. Vij, Jpn. J. Applied Phys. (Part 1), **33**, 2648 (1994).

[43] H. Xu, J. K. Vij, A. Rappaport and N. A. Clark, Phys. Rev. Lett. **79**, 249 (1997).

[44] A. Kocot, R. Wrzalik, J. K. Vij, M. Brehmer and R. Zentel, Phys. Rev B **50**, 16346 (1994).